Spatially confined and temporally resolved refractive index and scattering evaluation in human skin performed with optical coherence tomography

A. Knüttel
ISIS optronics GmbH
Innstr. 34
68199 Mannheim, Germany

M. Boehlau-Godau
Andersen Wohnpark 8
99834 Gerstungen, Germany

Abstract. In the present applications of optical coherence tomography (OCT), parameters besides pure morphology are evaluated in skin tissue under *in vivo* conditions. Spatially mapped refractive indices and scattering coefficients may support tissue characterization for research and diagnostic purposes in cosmetics/pharmacy and medicine, respectively. The sample arm of our OCT setup has been arranged to permit refractive index evaluation with little mechanical adjustment of a lens within the objective. A simple algorithm has been derived. Known from atmospheric work, the Klett algorithm [J. D. Klett, "Stable analytical inversion solution for processing LIDAR returns," Appl. Opt. **20**(2), 211–220 (1981)] has been applied to the same data set for retrieval of scattering coefficients. Both parameters have been measured in layered structures in skin like stratum corneum, epidermis and dermis. Significant water content in a localized sweat gland duct has been observed by refractive index evaluation. Time studies over 1.5 h permitted a first understanding about physiological changes in skin which are not obtainable by intrusive methods. © *2000 Society of Photo-Optical Instrumentation Engineers.* [S1083-3668(00)00801-7]

Keywords: OCT; refractive index; scattering coefficient; Klett algorithm; in vivo; skin; cosmetics; pharmacy; dermatology.

1 Introduction

Optical coherence tomography (OCT) becomes rapidly important in noninvasive medical diagnostics. This fairly new tool generates high resolution images of morphological microstructures in biological systems.[1] Numerous papers have been published. OCT has been applied to a wide range of retinal macular diseases.[2,3] It has been demonstrated that optically moderately scattering tissue of the body's interior such as the vascular system,[4] veins[5] and the gastrointestinal tract[6] can be imaged clearly with OCT. Highly scattering tissue like skin has also been imaged extensively.[7,8]

OCT works analogously to an ultrasound B scanner, except that ultrasound pulses are replaced by broadband light. The corresponding short coherence length permits spatial resolution in depth direction below 10 μm. The lateral resolution is given by the focusing power of the employed objective as long as single scattering prevails. The onset of multiple scattering limits high resolution to penetration depths not exceeding few 100 μm.[9,10] Depending on the scattering properties of tissue and some accepted loss in resolution, penetration depths of 1 mm or more can be achieved.

OCT is capable in probing other interesting parameters besides morphology in tissue. Water absorption has been evaluated by tuning the light source to an overtone band at 1.46 μm.[11] Birefringence for the characterization of ordered structures from collagen and elastin fibers has been exploited.[12,13] Doppler flow evaluation in combination with imaging becomes increasingly attractive because of the inherent sensitivity to frequency shifts in the detected OCT signals. Applications in a rodent model have been presented.[14]

Important parameters for tissue differentiation are the refractive index and scattering coefficients. Both parameters are related to each other in a complicated manner. The scattering coefficient is a consequence of the local refractive index distribution. Scattering coefficients have been computed based on a model of statistically varying binary index fluctuations which are treated as discrete particles with different sizes.[15] For homogeneous tissue and certain model parameters average scattering coefficients have been predicted as function of wavelength.

In literature, averaged refractive indices[16] and scattering coefficients[17] have been measured in skin with OCT, in each case assuming homogeneous condition within the entire region of interest. The next structural level in skin comprises the layers stratum corneum, epidermis and dermis (the subdermis is invisible to OCT). An even further refinement brings up laterally confined structures like sweat gland ducts. Due to the heterogeneous morphology and complicated physiology within the structures, an average parameter refractive index or scattering coefficient within an entire region is an oversimplification.

Averaging over an entire region of interest, however, has the technical advantage of reducing the variance of the de-

---

Address all correspondence to A. Knüttel, ISIS optronics GmbH, Innstr. 34, 68199 Mannheim, Germany. Electronic mail: a.knuettel@isis-optronics.de
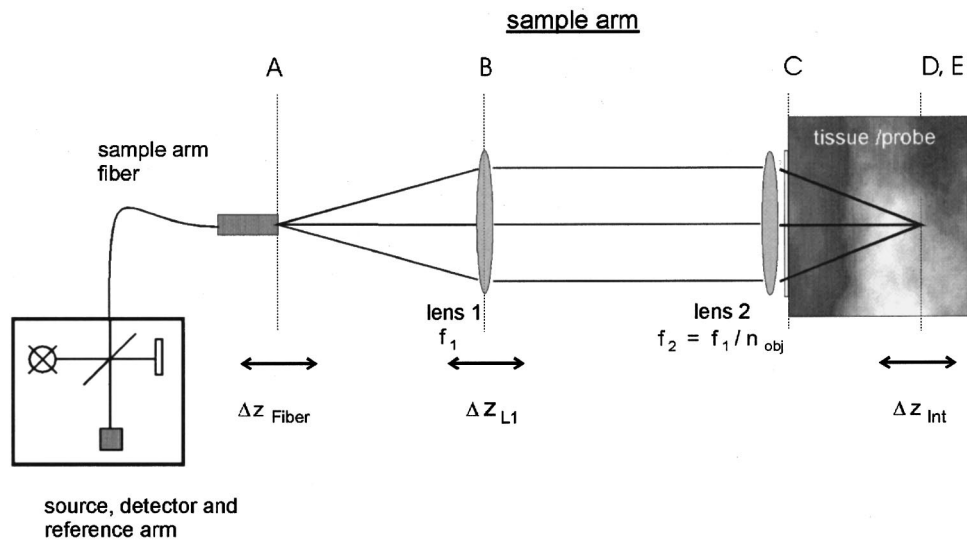
Fig. 1 Schematic of the sample arm of our OCT (mainly Michelson interferometer) setup. The main components in the sample arm are the moving fiber tip around position A and the lenses 1/2 within the objective. The position of lens 1 can be slightly altered to adjust for local deviations from an average refractive index. The other three arms of the interferometer (source, detector and reference arms) are schematically illustrated in the small box.

tected signals. Interference between backreflected signals from several points occurs within the coherence length along depth direction. Consequently, partially or even completely destructive interference signals—called speckles—arise. Under the worst-case assumption of completely developed (polarized) speckles, the variance of backscattered signals equals the signal itself.[18] Incoherent averaging of signal intensities over a spatial region is effective in reducing this variance.

The refractive index as average skin parameter has been measured *in vitro* and *in vivo* with OCT by Tearney et al.[16] Average refractive indices from *in vitro* dermis of $n \approx 1.41$, from *in vivo* stratum corneum of $n \approx 1.51$ and from *in vivo* epidermis of $n \approx 1.34$, have been measured in different settings and experiments. The basic approach presented in this paper was to adjust the reference mirror for maximum signal at a particular focus position within the sample. The relative distance of the reference mirror with regard to the sample position was exploited. This method has the disadvantage that reference mirror and tissue sample have to be moved relative to each other by distances comparable to the penetration depth which in turn precludes robust field employment. With a very similar setup, Haruna et al.[19] very recently determined the phase and group refractive indices in samples between glass plates to an accuracy of 0.3%.

The paper by Tearney et al.[16] gave a comprehensive overview about alternative methods for refractive index evaluation. These methods work only either with thin transparent layers or with homogenized tissue, precluding operation under *in vivo* conditions with highly scattering tissue.

The scattering coefficient as average parameter has been measured *in vivo* by Schmitt, Knüttel, and Bonner.[17] Average scattering coefficients of $\mu_s \approx 4.7$ mm^{-1} and $\mu_s \approx 1.2$ mm^{-1} were obtained from the dermis of a lower arm and the stratum corneum of an index finger. Averaging over several lateral positions was required to yield sufficient stability in the data.

The scope of this paper is to perform quantitative and simultaneous measurements of refractive indices and scattering coefficients within layered structures of skin and even local substructures like sweat gland ducts. The dynamic properties of both parameters have been monitored as well. The paper is organized as follows: In Sec. 2, the OCT setup for determining the refractive index is outlined. In Sec. 3.1, a simple formula for the refractive index evaluation has been derived. In Sec. 3.2, a principle known from the atmospheric community is employed to evaluate scattering coefficients in several layers. The experimental data including the images from the regions of interest are presented and discussed in Sec. 4. A summary and conclusion follows in Sec. 5.

2 OCT Setup

The basic OCT imaging setup for the simultaneous measurements of refractive indices and scattering coefficients is shown in Figure 1. The heart of the imaging setup consists of a Michelson interferometer, employing four optical arms. For a more detailed description about setup and functionality of OCT, the reader is referred to the literature.[1,7] The sample arm comprises the major hardware features for refractive index evaluation. The optical path in the reference arm remains constant, while only the distal tip of a fiber in the sample arm is moving.

Access to all three directions in the sample is achieved by moving the distal tip of a fiber around position A correspondingly. Diverging light emanating from the fiber is relayed through the objective comprising lens 1/lens 2 and refocused by lens 2 (at position C) into a point D, E within the sample. The scanning stage, where the fiber is attached, is not shown for simplicity. Optimal depth localization is achieved by (nearly) coincidence between the positions of the maxima of the interference pattern and the spatial focus within the sample. This condition is depicted in Figure 2(a). The position
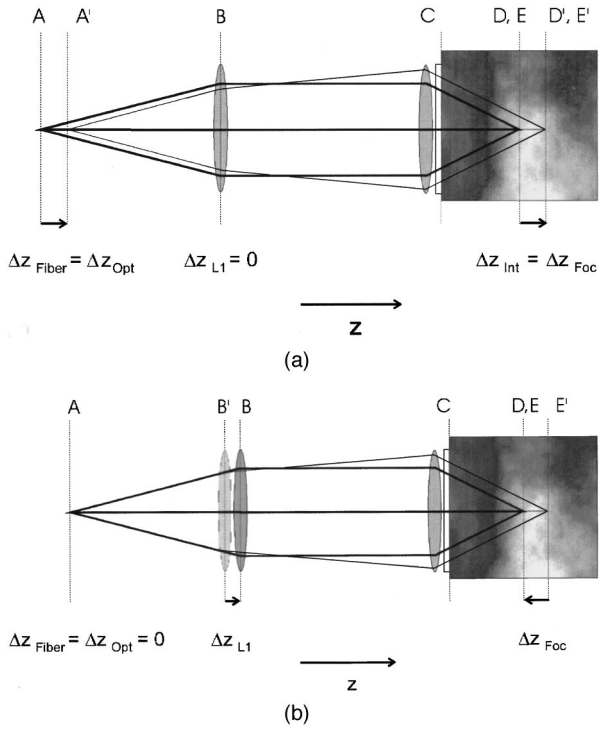
Fig. 2 (a) The positions of the interference pattern maximum (D,D′) and the spatial focus (E,E′) coincide. Changes in position of the fiber tip from A to A′ alter the coinciding maxima correspondingly. The refractive index of the medium was assumed to be $n_{med}=n_{obj}$ [see Eq. (2) in text] to keep the position of lens 1 constant ($\Delta z_{L1}=0$). (b) Impact of the position of lens 1 on the spatial focus at fixed fiber position A. To achieve coincidence between the maxima of the spatial focus and the interference pattern, lens 1 has to be moved (from B′ to B) to shift the spatial focus from E′ to E depending on the refractive index of the medium. The position of the maximum of the interference pattern (at D) is unaffected.

D of the interference pattern maximum is given by the matching condition of the optical paths in the sample and reference arm for a given position A. The position E of the spatial focus is determined by the transfer function of the objective. Under certain conditions for the focal lengths of the lenses and the (average) refractive indices of the sample, moving only the fiber tip to a new position shifts both maxima in coincidence, implying that the spatial focus is tracked.

The principle of focus tracking is illustrated in Figure 2(b). The coincidence between the maxima of the interference pattern (D) and spatial focus (E) is ensured by moving lens 1 from position B′ to B (moving E′ to E). For refractive indices of a sample medium being within the physiological range, a repositioning within a few μm is sufficient to achieve coincidence (D=E). Please note that all unprimed focus positions indicate coincidence of both maxima, or focus tracking. The setup in the sample arm resembles that of Lexer et al.[20] but their paper did not uncover any adjustments necessary to correct for local refractive index fluctuations.

The subsequent collection of equations describes resolution issues regarding the interference pattern and spatial focus. Spatial resolution in axial direction or full width at half maximum (A-FWHM) of the interference pattern in depth is given by[3]

$$A\text{-FWHM}_{Int}=\frac{2\cdot\ln(2)}{\pi}\cdot\frac{\lambda_0^2}{\Delta\lambda\cdot n_{med}},\qquad(1)$$

where λ_0 is the employed center wavelength, $\Delta\lambda$ is the bandwidth of the light source and n_{med} is an assumed homogeneous refractive index of the sample medium. A-FWHM$_{Int}$ (at D) determines the spatial resolution as long as (a) A-FWHM$_{Foc}$ (at E) is comparably large and (b) both maxima approximately coincide. Given the ratios of the focal lengths f_1/f_2 and numerical apertures NA_2/NA_1 in the paraxial regime (small NA) by

$$n_{obj}=\frac{f_1}{f_2}\approx\frac{NA_2}{NA_1},\qquad(2)$$

we obtain[21]

$$A\text{-FWHM}_{Foc}=\frac{2}{\pi}\cdot\frac{n_{med}\cdot\lambda_0}{NA_2^2}.\qquad(3)$$

An ideal objective without aberrations has been assumed for the validity of Eq. (3).

The lateral resolution is entirely determined by the spatial focusing power of the objective. Including Eq. (2), we obtain the lateral FWHM to be[21]

$$L\text{-FWHM}_{Foc}=\frac{2}{\pi}\cdot\frac{\lambda_0}{NA_2}.\qquad(4)$$

The performance data of our OCT system regarding spatial resolution and field of view are as follows: a bandwidth of $\Delta\lambda=70$ nm and a center wavelength of $\lambda_0=1300$ nm generated an A-FWHM$_{Int}=7.4$ μm according to Eq. (1). An average refractive index of the sample medium $n_{med}=n_{obj}=1.43$ has been assumed. The spatial counterpart is A-FWHM$_{Foc}=34$ μm according to Eq. (3) and thus large compared to A-FWHM$_{Int}$. The numerical aperture of the standard fiber equals the one of lens 1 being $NA_1=0.13$. According to Eq. (4), the diffraction limited lateral resolution yields L-FWHM$_{Foc}=4.5$ μm. For a two-dimensional image, the field of view covers almost 1 mm in depth and 1.2 mm in one lateral direction. To improve signal accuracy by averaging during *in vivo* experiments, eight two-dimensional data sets were acquired along the third (second lateral) direction. These three-dimensional data sets were obtained within 5 min each.

3 Theory

For the subsequent description of the formulas regarding refractive index and scattering coefficients, strictly single scattering has been assumed. Even though it is known that multiple scattering arises at depths exceeding few 100 μm, no attempt for corresponding correction has been made. Absorption and polarization have been neglected throughout the paper.

3.1 Refractive Index Evaluation

For the refractive index evaluation, the coincidence of the maxima of the interference pattern and spatial focus is of importance. At least two points along the depth direction have to be probed to evaluate a mean value in between. Subse-

quently a formula is derived to evaluate the refractive index from axial position changes of the fiber tip and lens 1 within the sample arm.

The optical path length Δz_{opt} in an assumed homogeneous medium is proportional to the group refractive index n_g and the geometrical path length Δz_{Int} given by the distance from point D to D' [see Figure 2(a)]

$$\Delta z_{opt} = n_g \cdot \Delta z_{Int}. \qquad (5)$$

It is important to note that regarding only the interference condition, changes around position B of lens 1 do not affect Eq. (5) (in the limit of small NAs).

For a given position of lens 1 (B), moving the fiber tip around A alters the focus position E accordingly. The relative change due to the fiber tip Δz_{fiber}, the lens 1 Δz_{L1}, and the focus Δz_{Foc} lead to the relationship

$$\Delta z_{Fiber} = \Delta z_{L1} + \Delta z_{Foc} \cdot \frac{n_{obj}^2}{n_p}, \qquad (6)$$

where n_p is the phase index of the medium. Given Snell's law for refraction of wave fronts, Eq. (6) is only valid for small NAs. As a reminder, the ratio n_{obj} is calculated according to Eq. (2).

To achieve maximum signal, the maxima of the interference pattern and spatial focus have to coincide. Consequently, the condition $\Delta z_{Int} = \Delta z_{Foc}$ has to be fulfilled. The change of the fiber position corresponds to a change in optical path-length yielding $\Delta z_{Fiber} = \Delta z_{opt}$. Substitution of Eq. (5) into Eq. (6) and solving for the refractive index yields

$$\bar{n} = \sqrt{n_g \cdot n_p} = \frac{n_{obj}}{\sqrt{1 - (\Delta z_{L1} / \Delta z_{Fiber})}}. \qquad (7)$$

The mean refractive index $\bar{n}$ is the geometrical average of the phase and group index. The difference between both indices is usually a few percent[16] and sufficiently small to be ignored for further treatment, where we simply refer to the refractive index n (omitting the bar) in Eq. (7). For a piecewise homogeneous medium along the depth direction, the slope $\Delta z_{L1} / \Delta z_{opt} = \Delta z_{L1} / \Delta z_{Fiber}$ has to be evaluated.

In Figure 3 the normalized detector current signal versus relative change in position of lens 1 is displayed for different targets. Near zero position, all targets experience a more or less pronounced maximum, implying that the maxima at the interference pattern and axial spatial focus coincide. In the case of a flat glass plate, the signal adjacent to the maximum drops faster than in the epidermis and dermis. For a qualitative explanation, skin can be regarded as a heterogeneous ensemble of point scatterers. It has been shown that point scatterers generate a shallower focus than perfect flat targets.[9] The deeper the penetration into tissue, the more shallow is the focus curve. The quality of the shape of the focus curve arising from the dermis is compromised due to heterogeneity. The flatness compared to the epidermis curve might be an indication of the onset of multiple scattering. The sharper the focus curve and the better the quality of the shape around the maximum, the more accurate is the retrieval of parameter Δz_{L1} and consequently the evaluation of the refractive index n. An ad-
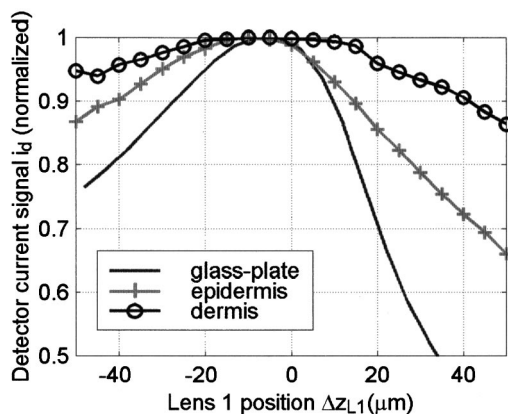

Fig. 3 Typical detector-signal curves i_d for several positions Δz_{L1} of lens 1. The maximum of each curve indicates a coincidence between the maxima of the spatial focus and the interference pattern. To increase signal accuracy, all values along the lateral direction of the corresponding data sets have been averaged. The slight asymmetry within the curves may arise due to imperfect objective conditions.

vantage of this method is the evaluation of absolute values with inherent insensitivity to light sources intensities.

The goal was to verify the refractive index of a homogeneous water suspension. In Figure 4, spheres with 1 μm in diameter and 0.8% concentration have been imaged with OCT. Fairly strong speckle signals appear because no averaging has been performed. The displayed field of view is 500 μm in depth and 1.2 mm in lateral direction. The signal decays at about 400 μm optical depth (corresponding to a geometrical depth of 400 μm/1.33=300 μm) down to the noise floor. The abscissa axis displays the position change to lens 1. To ensure sufficient signal accuracy, an optical depth range of 300 μm was selected and the lateral values were averaged. According to the fitted slope $\Delta z_{L1} / \Delta z_{Fiber} \approx -50$ μm/300 μm the refractive index can be calculated to
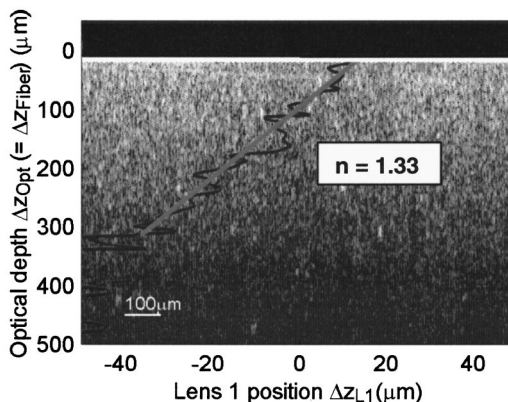

Fig. 4 OCT image of a water suspension of polymethylenmelanin spheres ($\varnothing$=1 μm). The lateral extend is 1.2 mm. The bright horizontal line corresponds to a glass plate (plane C in Figure 1). The wavy focus curve shows the actual position Δz_{L1} vs optical depth Δz_{opt} of lens 1 under the condition of coincidence of both maxima [cf. Figure 2(b)]. All signal data along the lateral direction have been averaged. By fitting the focus curve with the straight slope, a refractive index of n =1.33 was obtained according to Eq. (7).
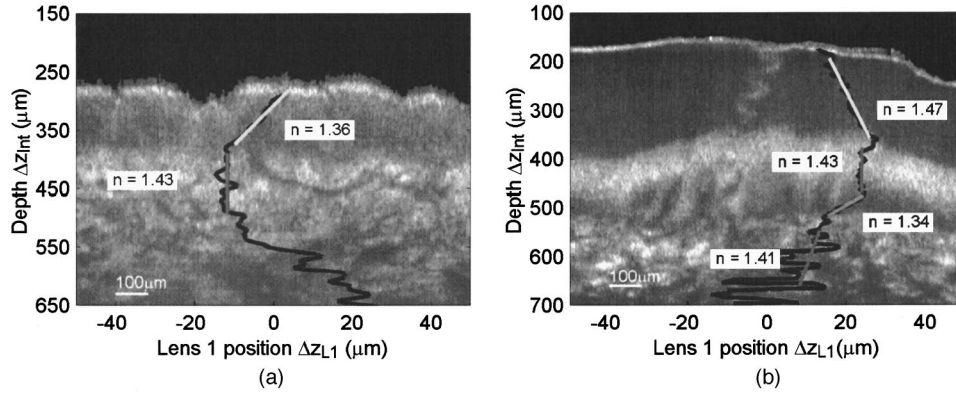
Fig. 5 OCT images of (a) the volar side of a lower arm and (b) the palm of a hand. The lateral extent of each image is 1.2 mm. The wavy curves show the actual positions Δz_{L1} vs geometrical depths $\Delta z_{int} = \Delta z_{opt}/n_{obj}$ of lens 1 under the condition of coincidence of both maxima [cf. Figure 2(b)]. All signal data along the lateral direction have been averaged. Within the piecewise homogeneous skin layers, the fitted slopes yield the corresponding refractive indices according to Eq. (7). The assignment of the layers is comprised by the curved nature but it can be approximated as follows: (a) epidermis (first slope) and upper dermis (second slope); (b) stratum corneum (first slope), granular layer of epidermis (second slope), basal layer of epidermis (third slope) and upper dermis (fourth slope).

$n \approx 1.33$ according to Eq. (7). This value agrees fairly well with the geometric mean of n_p and n_g $(>n_p)$ of water at 1300 nm.

The ratio of the focal lengths [cf. Eq. (2)] of both lenses has been set to $n_{obj} = 1.43$ because it was assumed to match an average refractive index n_{med} in skin tissue. It will be shown later than in spite of the heterogeneity of skin such average value is justified. Only in the particular case where n_{med} exactly matches n_{obj}, the position of lens 1 is unaltered, thus $\Delta z_{L1} = 0$. Around this operating position the sensitivity is highest for changes in refractive index.

3.2 Scatter Coefficient Evaluation

For evaluating the scattering coefficient, the original algorithm presented by Klett[22] was adapted. This algorithm employed for processing atmospheric [light detecting and ranging (LIDAR)] signals is based on assuming purely single scattering.

Assuming the following relationship between the volume backscatter $\beta(z)$ and the scattering coefficient $\sigma(z)$:

$$\beta(z) = \text{const} \cdot \sigma(z)^k, \tag{8}$$

Klett presented the following stable analytic solution[22]:

$$\sigma(z) = \frac{\exp[(S(z) - S(z_{max}))/k]}{\sigma(z_{max})^{-1} + 2/k \cdot \int_z^{z_{max}} \exp[(S(z') - S(z_{max}))/k] \cdot dz'}. \tag{9}$$

For LIDAR systems $S(z) = \ln(z^2 \cdot P(z))$ is the logarithmic range-adjusted power where z is the distance between scatterer and detector and $P(z)$ the received power. For the OCT device $S(z)$ has to be modified to $S(z) = \ln(\alpha(NA) \cdot i_d^2(z))$, where $i_d(z)$ is the measured (ac−) detector current from light captured at a given fiber position z. The function $\alpha(NA)$ takes the numerical aperture NA into account. Since NA is effectively changing only slightly, $\alpha(NA)$ can be considered constant. Given this assumption and setting $k = 1$, Eq. (9) can be written as

$$\sigma(z) = \frac{i_d^2(z)}{\sigma(z_{max})^{-1} \cdot i_d^2(z_{max}) + 2 \cdot \int_z^{z_{max}} i_d^2(z') \cdot dz'}. \tag{10}$$

The scattering coefficient $\sigma(z)$ can be calculated from $z = z_{max}$ up to the surface $z = 0$. Notice that $\sigma(z_{max})$ is generally unknown and has to be estimated. For $z < z_{max}$ the integral becomes the dominant part of the denominator and $\sigma(z)$ approaches exact values even for wrong estimates of $\sigma(z_{max})$. Theoretical simulations and evaluation of OCT data showed that overestimation of $\sigma(z_{max})$ approaches the results better than underestimation. Even if $\sigma(z_{max})$ is estimated twice as big as the real value, the error for $\sigma(z)$ can be neglected 100 μm above z_{max}, according to measurements in homogeneous phantoms.

4 *In vivo* Skin Measurements

Subsequently, evaluated refractive indices and scattering coefficients are presented after being obtained from *in vivo* measurements in volunteers. Generally three-dimensional data sets were acquired to provide sufficient signal averaging within a region of interest. In Sec. 4.1, refractive indices and scattering coefficients from various layers in skin will be presented. A pronounced local structure is shown in Sec. 4.2 to demonstrate further confinement capabilities in refractive index evaluation. Time dependent studies regarding refractive indices and scattering coefficients conclude Sec. 4 (Sec. 4.3).

4.1 Layered Structures

Three-dimensional data sets have been acquired from the volar side of the arm and the palm of a hand. To reduce the speckle appearance in all subsequent images to a large extent, images acquired along the third dimension (with 5 μm interplane distance) were averaged to generate smoothed two-dimensional images, as shown in Figure 5. Signal accuracy has priority over compromised spatial resolution. The (geometrical) field of view along the depth is limited to about 600 μm. The lateral field of view is always 1.2 mm.

Table 1 The averaged refractive indices of various layers from the images shown in Figures 5(a), volar side of a lower arm, and Figure 5(b), palm of a hand from one volunteer, are condensed with corresponding uncertainties.

Refractive indices n	Volar side of lower arm	Palm of hand
Stratum corneum	⋯	1.47±0.01
Epidermis	1.36±0.01	1.43±0.02 (Granular layer)
		1.34±0.02 (Basal layer)
Upper dermis	1.43±0.02	1.41±0.03

Refractive indices and scattering coefficients have been evaluated from the images in Figure 5. For visualization regarding the refractive index computations, the abscissa of the images depict the position changes of lens 1. The actual position Δz_{L1} versus depth of lens 1 is derived from the laterally averaged signal. Along a quasihomogeneous layer, slopes were fitted to the focus curves to obtain the averaged refractive indices according to Eq. (7). The increasing uncertainty with depth arises from perturbed focus curves (cf. Figure 3). Thus confident data are, at present, restricted to depths not exceeding 400 μm.

Figure 5(a) shows the averaged image (along the third dimension) of a lower arm at the volar side. The uppermost layer, the stratum corneum, has a thickness of only 10–20 μm which is too small for a meaningful refractive index evaluation (at least at the present state of our OCT technology). The next layer is the epidermis at about 100 μm layer thickness. The upper part of the dermis beneath is the deepest layer from where meaningful refractive index values can be retrieved. Figure 5(b) shows an averaged image of the palm of a hand. The upper layer of about 200 μm thickness corresponds to the stratum corneum. The adjacent layer is possibly the granular (and spinous) part of the malpighian layer. The basal layer might be assigned to the dark and slightly corrugated curved

band.[23] Below the layers of the epidermis, the upper part of the dermis is visible due to strongly backreflecting signal. The evaluated average refractive indices with corresponding uncertainties are condensed in Table 1. The uncertainties are determined by (a) curved and corrugated layers (independent of depth) and (b) poor accuracy in the retrieval of the position Δz_{L1} of lens 1 with increasing depth.

In contrast to Figure 4, in Figure 5 the geometrical depths of the images are shown. To facilitate computation, the optical lengths have been divided by an assumed mean refractive index according to $\Delta z_{int} = \Delta z_{opt}/n_{obj}$. It should be pointed out, however, that the actual geometrical value may differ at various depths by as much as 3%–4% due to the local refractive index variations.

In Figure 6, the scattering coefficients σ along the depth obtained from two volunteers are displayed. For the evaluation of the scattering coefficients according to Eq. (10) certain assumptions have been made as outlined in Sec. 3.2. To improve signal-to-noise ratio, values along the lateral direction have been averaged.

The scattering curves along the depth are distinctly different for various measured sites. (a) At the volar side of a lower arm [Figure 6(a)], σ drops to small values in the epidermis and rises at the epidermal/dermal border and upper dermis. Beyond 400 μm depth, σ drops again to fairly constant values. At the palm of the hand [Figure 6(b)], the extended stratum corneum exhibits a small σ. The decline within the stratum corneum could be the result of the assumption for $k = 1$. In the granular layer σ rises significantly. Behind a small drop within the basal layer, σ rises again to fairly constant values within the dermis depending on the individual skin characteristics. The approximate σ values were assigned to the same layers as for Figure 5 and condensed in Table 2. The uncertainties are given by the individual skin characteristics and the assumptions made.

As outlined in Sec. 3.2, the Klett algorithm for evaluation of the scattering coefficients requires a start value at the deepest end of the data curve. In the initial phase of the retrieval such values have to be guessed. In Figure 6(b), however, it is demonstrated that the curves at the ''correct'' and twice the
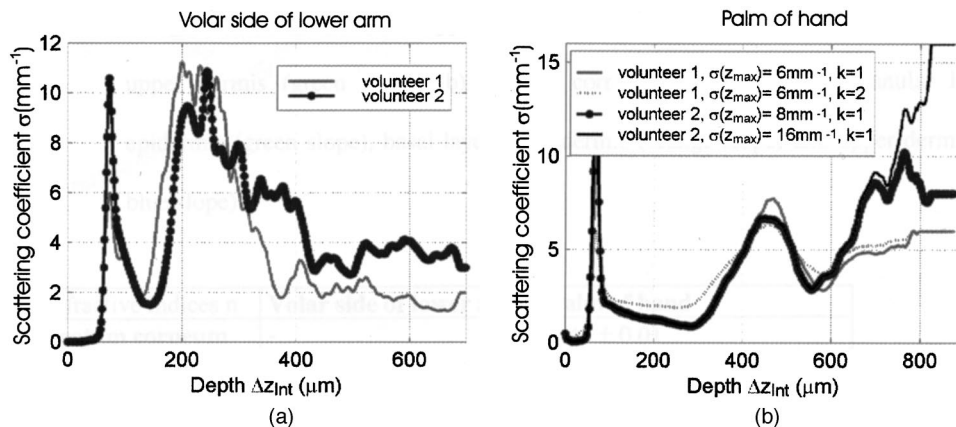
Fig. 6 From the data set of Figure 5(a) the volar side of a lower arm and (b) the palm of a hand of volunteer 1, the corresponding scattering coefficients along geometrical depth $\Delta z_{int} = \Delta z_{opt}/n_{obj}$ have been computed according to Eq. (10). Data from volunteer 2 are shown for comparison. As for the refractive index evaluation, all lateral data have been averaged. In (b) the evaluated scattering coefficient curves for different k and $\sigma(z_{max})$ are depicted (cf. text).

Table 2 Approximate scattering coefficients of various layers, condensed from the curves shown in Figure 6(a), volar side of a lower arm, and Figure 6(b), palm of a hand.

Scattering coefficients σ (mm^{-1})	Volar side of lower arm	Palm of hand
Stratum corneum	$\cdots$	1–1.5
Epidermis	1.5–2	6–7 (Granular layer)
		4–5 (Basal layer)
Upper dermis	8–10	5–8

correct start value merge within 100–200 μm down from the deepest measured point z_{max} of the tissue. It is possible to get a good estimate for the scattering coefficient within approximately the first 500 μm in skin, which underlines the robustness of the Klett algorithm, even under *in vivo* conditions.

4.2 Local Structures

Skin layers are generally inhomogeneous in lateral and depth direction. Local structures like sweat gland ducts and vessels can significantly alter the physical properties within layers. Subsequently the impact on refractive indices is studied.

In Figure 7 the image of the thumb of a volunteer is displayed twice pointing to two different processing scenarios. As for Figure 5, the lateral extent of the images is 1.2 mm and the actual positions Δz_{L1} of lens 1 are depicted. Within the stratum corneum, the fitted slope of the focus curve yielded an averaged refractive index of $n = 1.46$ [Figure 7(a)]. The entire lateral direction has been averaged, including the signals from the sweat gland ducts.

In Figure 7(b) only the signals from the area around the right sweat gland duct have been averaged. In the upper part of the stratum corneum the duct is fairly well visible. Here a low refractive index of 1.37 has been retrieved, indicating that sweat comprises a significant amount of water. In deeper areas the duct fades from the selected (average) plane and the

average refractive index rises to 1.43. Still a small amount of water seems to be contributing to the average value. Given the smaller lateral range for averaging, the uncertainty of the focus curve rises as compared to the one in Figure 7(a).

4.3 Time Series

Provided that averaging across the entire lateral extent is possible, we are able to retrieve refractive indices n to better than 1% *in vivo* within a time slice of 5 min at the present stage of our OCT technology. Due to this fairly high accuracy within a reasonable time slice, we were encouraged to conduct a series of data sets to study effects of n over a time span of up to 1.5 h. The same data sets were used to retrieve scattering coefficients σ over time.

In Figure 8 the images from the thumb of a volunteer are displayed, obtained at time 0 min [Figure 8(a)] and 80 min [Figure 8(b)], respectively. The axes are denoted as in the previous images. The ''perturbing'' effects of sweat gland ducts have been demonstrated in the previous section and excluded for the refractive index evaluation. The fitted slopes of the focus curves yielded a decline within the stratum corneum from $n = 1.46$ to $n = 1.445$ within 80 min. A possible explanation is that increasing moisture content from sweat ''dilutes'' the average refractive index.

Interesting to note are changes in morphology in the stratum corneum over time. In Figure 8(a) the original thickness (0 min) is marked by few white arrows. After 80 min a swelling can be observed in Figure 8(b). The marks indicate an average thickness increase of 30–40 μm. This fact may support the aforementioned explanation of a volume effect by increasing moisture content.

In Figure 9, the refractive indices of the epidermis [Figure 9(a)] and stratum corneum [Figure 9(b)] from the thumbs of two volunteers are retrieved in 5 min intervals over a time course of maximal 90 min. As for Figure 8, sweat gland ducts have been excluded from data processing. A consistent decline over time can be observed for both layers. Occasional disruptions in the smoothness of the curves can be explained by yet insufficient data averaging in very heterogeneous tissues.
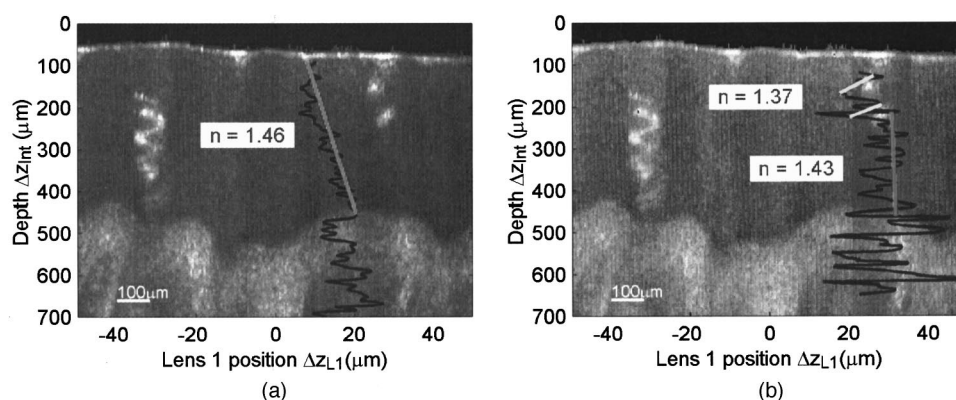
Fig. 7 Refractive indices of the stratum corneum, obtained (a) along the entire lateral extend (1.2 mm) and (b) from the laterally confined area around the right sweat gland duct (about 0.2 mm). The procedure for the refractive index evaluation was described for Figure 5. The sweat gland duct (b) exhibits a lower refractive index than the average stratum corneum. Due to the reduced lateral averaging capabilities, the uncertainty in the data is increased.
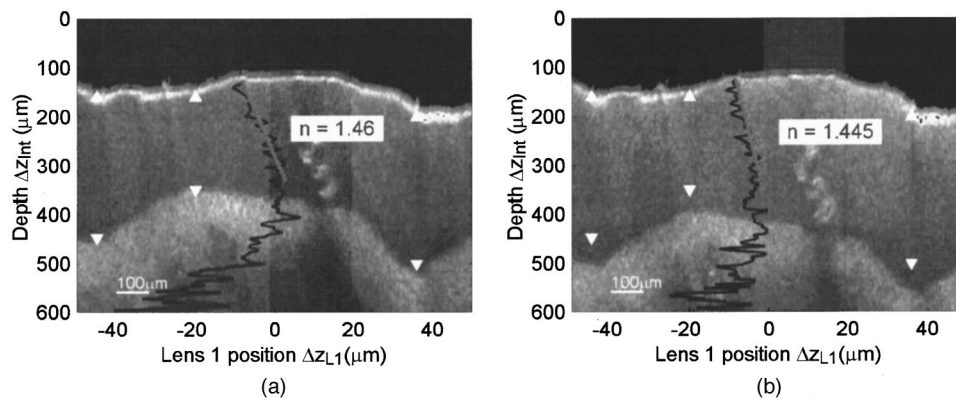
Fig. 8 Refractive indices of the stratum corneum of the palm of a hand, obtained (a) at 0 min and (b) after 80 min. The procedure for the refractive index evaluation was described for Figure 5. After 80 min (b) a measurable decrease in refractive index is observed. In addition the stratum corneum swells by 30–40 μm (see arrows, which are positioned identical in both images). The shaded areas of the images—incorporating a sweat gland duct—have been excluded in the evaluation due to the findings in Figure 7.

In Figure 10, the scattering coefficients of the epidermis [Figure 10(a)] and stratum corneum [Fig. 10(b)] were obtained from the same data sets as for Figure 9. In the stratum corneum, the scattering coefficients consistently rise over time by up to 40%. This effect can possibly be explained by swelling of dense and ''dried'' corneocytes[23] causing local differences in refractive indices to increase. The drop of the scattering coefficients in the epidermis over time by about 5% could not be explained.

5 Summary and Conclusion

A setup has been devised in which the spatial focus and the interference condition coincide at a predetermined average refractive index n_{med} of the sample, independently of the position Δz_{Fiber} of the fiber tip which causes the depth scanning. Coincidence can be achieved by setting the ratio of the focal lengths of the two lenses within the sample arm objective to $n_{obj} = n_{med}$. Deviation from n_{med} can be tracked by position changes Δz_{L1} of lens 1 to maximize the (averaged) signal. In the performed *in vivo* experiments penetrating more than 500 μm, changes by $\Delta z_{L1} \leqslant \pm 30$ μm were sufficient to cover the range of physiological refractive indices.

A simple algorithm for refractive index evaluation has been derived. Within a sufficiently homogeneous field of view, after lateral averaging the data, only the slope $\Delta z_{L1} / \Delta z_{Fiber}$ has to be measured to retrieve the corresponding averaged refractive index n. Known from atmospheric LIDAR experiments, the Klett algorithm[22] has been adapted for retrieval of scattering coefficients σ. A simple relationship between forward and backward scattering ($k=1$) in tissue has been assumed.

Average refractive indices and scattering coefficients have been evaluated *in vivo* within layers like stratum corneum, epidermis and dermis (upper part). At thicknesses around 100 μm, refractive indices were obtained with accuracies of better than ± 0.01 close to the surface. The measured values are consistent with the ones published by Tearney et al.[16]

Local refractive indices of sweat gland ducts have also been retrieved. Even though the accuracy has been compromised due to a smaller ''homogeneous'' field of view, clearly an increased water content from sweat could be observed.

Time series over 1.5 h have been conducted to follow changes in refractive index and scattering coefficients under stable *in vivo* conditions. Within the layers epidermis and stra-
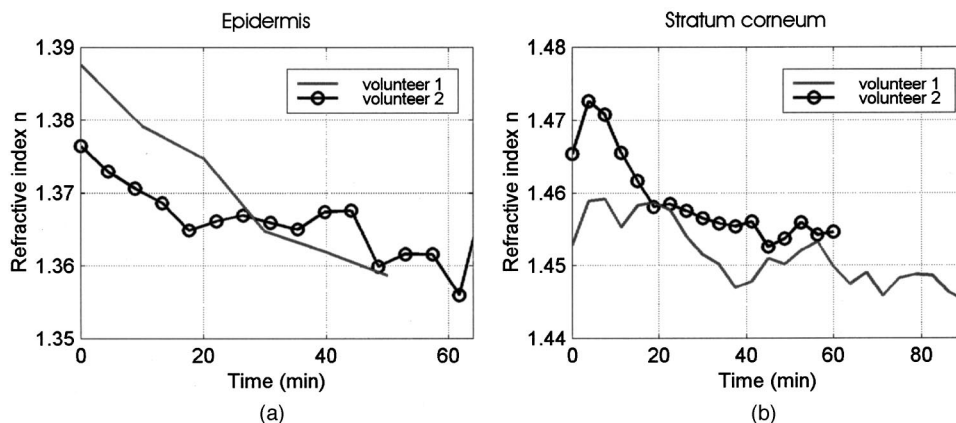
Fig. 9 Refractive index measurements over time, within the (a) epidermis of the volar site of a lower arm and (b) stratum corneum of the palm of a hand. The corresponding original data sets (from volunteer 1) stem from the one for Figure 5.
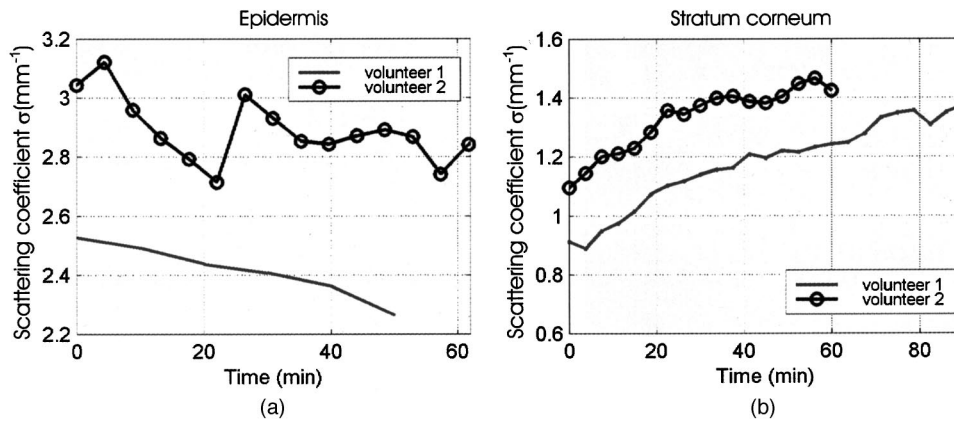
Fig. 10 Scatter coefficient measurements over time, within the (a) epidermis of the volar site of a lower arm and (b) stratum corneum of the palm of a hand. The corresponding original data sets (from volunteer 1) stem from Figure 5 and the processed ones from Figure 6.

tum corneum (at a thumb), the refractive indices decline over time. In parallel, the scattering coefficients drop in the epidermis and rise in the stratum corneum. The behavior in the stratum corneum can possibly be explained by moisture uptake from sweating.

In strongly heterogeneous tissue the field of view for retrieval of homogeneous refractive indices has to be small. Detrimental is the strong speckle appearance in unaveraged OCT images. Remedy is extense signal averaging along the second lateral dimension. Local three-dimensional data sets with less than 50 μm length per dimension may be realistic to achieve average refractive indices of accuracies smaller than 0.01.

The Klett algorithm for scattering coefficients σ has been proven very stable to falsely guessed initial start values. A problem yet is the unknown and locally changing relation between forward and backward scattering. We verified that local alteration of the factor k from unity renders some σ values more meaningful.

Beyond a high resolution morphology in the OCT images, tissue characterization by additional local physical parameters can be desired for the cosmetics and pharmaceutical industry. Applications of cremes, oils, etc., will likely have an impact on parameters like refractive index and scattering coefficient, because the impact of moisture has been demonstrated in this study. In particular time studies with the nonintrusive diagnostic method OCT may provide, for the first time, the opportunity to observe subtle changes *in vivo*.

Acknowledgments

References

1. D. Huang, E. A. Swanson, C. P. Lin, J. S. Schuman, W. G. Stinson, W. Chang, M. R. Hee, T. Flotte, K. Gregory, C. A. Puliafito, and J. G. Fujimoto, ''Optical coherence tomography,'' *Science* **254**, 1178–1181 (1991).
2. A. F. Fercher, C. K. Hitzenberger, W. Drexler, G. Kamp, and H. Sattmann, ''In vivo optical coherence tomography,'' **116**, 113–114 (1993).
3. M. R. Hee, J. A. Izatt, E. A. Swanson, D. Huang, C. P. Lin, J. S. Schuman, C. A. Puliafito, and J. G. Fujimoto, ''Optical coherence tomography of the human retina,'' *Arch. Ophthalmol. (Chicago)* **113**, 325–332 (1995).
4. J. G. Fujimoto, M. E. Brezinski, G. J. Tearney, S. A. Boppart, B. E. Bouma, M. R. Hee, J. F. Southern, and E. A. Swanson, ''Optical biopsy and imaging using optical coherence tomography,'' *Nature Med.* **1**, 970–972 (1995).
5. G. J. Tearney, S. A. Boppart, B. E. Bouma, M. E. Brezinski, N. J. Weissmann, J. F. Southern, and J. G. Fujimoto, ''Scanning single-mode optic catheder-endoscope for optical coherence tomography,'' *Opt. Lett.* **21**(7), 543–545 (1996).
6. A. Sergeev, V. Gelikonov, G. Gelikonov, F. Feldchtein, R. V. Kuranov, N. Gladkova, N. M. Shakhova, L. B. Snopova, A. V. Shakhov, I. A. Kuznetzova, A. N. Denisenko, V. V. Pochinko, Yu. P. Chumakov, and O. S. Streltzova, ''In vivo endoscopic OCT imaging of precancer and cancer states of human mucosa,'' *Opt. Express* **1**(13), 432–440 (1997).
7. J. M. Schmitt, M. Yadlowsky, and R. F. Bonner, ''Subsurface imaging of living skin with optical coherence tomography,'' *Dermatology* **191**, 93–98 (1995).
8. J. Welzel, E. Lankenau, R. Birngruber, and R. Engelhardt, ''Optical coherence tomography of the human skin,'' *J. Am. Acad. Dermatol.* **37**, 958–963 (1997).
9. A. Knüttel, R. Schork, and D. Böcker, ''Analytical modeling of spatial resolution curves in turbid media acquired with optical coherence tomography (OCT),'' *Proc. SPIE* **2655**, 258–270 (1996).
10. J. M. Schmitt and A. Knüttel, ''Model of optical coherence tomography of heterogeneous tissue,'' *J. Opt. Soc. Am. A* **14**(6), 1231–1242 (1997).
11. J. M. Schmitt, S. H. Xiang, and K. M. Yung, ''Differential absorption imaging with optical coherence tomography,'' *J. Opt. Soc. Am. A* **15**, 2288–2296 (1998).
12. M. R. Hee, D. Huang, E. A. Swanson, and J. G. Fujimoto, ''Polarization-sensitive low-coherence reflectometer for birefringence characterization and ranging,'' *J. Opt. Soc. Am. A* **9**, 903–908 (1992).
13. J. F. De Boer, T. E. Milner, M. J. C. van Gemert, and J. S. Nelson, ''Two-dimensional birefringence imaging in biological tissue by polarization-sensitive optical coherence tomography,'' *Opt. Lett.* **22**, 934–936 (1997).
14. Z. Chen, T. E. Milner, X. Wang, S. Srinivas, and J. S. Nelson, ''Optical doppler tomography: Imaging in vivo blood flow dynamics following pharmacological intervention and photodynamic therapy,'' *Photochem. Photobiol.* **67**, 1–7 (1998).
15. J. M. Schmitt and G. Kumar, ''Optical scattering properties of soft tissue: A discrete particle model,'' *Appl. Opt.* **37**(13), 2788–2797 (1998).
16. G. T. Tearney, M. E. Brezinski, J. F. Southern, B. E. Bouma, M. R. Hee, and J. G. Fujimoto, ''Determination of the refractive index of highly scattering human tissue by optical coherence tomography,'' *Opt. Lett.* **20**(21), 2258–2260 (1995).
17. J. M. Schmitt, A. Knüttel, and R. F. Bonner, ''Measurement of opti-

cal properties of biological tissues by low-coherence reflectometry,'' *Appl. Opt.* **32**(30), 6032–6042 (1993).

18. J. W. Goodman, in *Laser Speckle and Related Phenomena*, J. C. Dainty, Ed., Springer, Berlin (1984).

19. M. Haruna, M. Ohmi, T. Mitsuyama, H. Tajiri, H. Maruyama, and M. Hashimoto, ''Simultaneous measurement of the phase and group indices and the thickness of transparent plates by low-coherence interferometry,'' *Opt. Lett.* **23**(12), 966–968 (1998).

20. F. Lexer, A. F. Fercher, H. Sattmann, W. Drexler, and S. Molobny, ''Dynamic coherent focus for transversal resolution enhancement of OCT,'' *Proc. SPIE* **3251**, 85–90 (1998).

21. Klein–Furtak, *Optik*, Springer, Berlin (1988).

22. J. D. Klett, ''Stable analytical inversion solution for processing LIDAR returns,'' *Appl. Opt.* **20**(2), 211–220 (1981).

23. Montagna–Kligman–Carlisle, *Atlas of Normal Human Skin*, Springer, New York (1992).